Metasurface perfect absorber based on guided resonance of a photonic hypercrystal

You-Chia Chang, Alexander V. Kildishev, Evgenii E. Narimanov, and Theodore B. Norris

Metasurface perfect absorber based on guided resonance of a photonic hypercrystal

You-Chia Chang,[1,2,*] Alexander V. Kildishev,[3] Evgenii E. Narimanov,[3] and Theodore B Norris[1,4]

[1]*Center for Photonics and Multiscale Nanomaterials, University of Michigan, Ann Arbor, Michigan 48109, USA*
[2]*Department of Physics, University of Michigan, Ann Arbor, Michigan 48109, USA*
[3]*School of Electrical and Computer Engineering and Birck Nanotechnology Center, Purdue University, West Lafayette, Indiana 47907, USA*
[4]*Department of Electrical Engineering and Computer Science, University of Michigan, Ann Arbor, Michigan 48109, USA*

By exploiting the guided resonance of a photonic hypercrystal - a periodic structure that combines the properties of hyperbolic materials and photonic crystals - we numerically demonstrate a perfect absorber consisting of a photonic hypercrystal slab, a dielectric spacer and a back reflector. The guided resonance of the photonic hypercrystal slab creates a field enhancement and confinement within a deep subwavelength thickness; therefore, the ultra-thin photonic hypercrystal slab serves as a two-dimensional resonator that can be treated accurately as a metasurface. We show that the perfect absorber is equivalent to a metasurface Salisbury screen, where the metasurface formed by the photonic hypercrystal slab provides the appropriate electric sheet conductivity required for critical coupling. We also present examples of combining the perfect absorber with graphene to make optical modulators and to improve the absorption in graphene photodetectors.

INTRODUCTION

Absorbers are of great interest to technologies of detectors, sensors, solar cells, stealth, optical modulators and thermal emitters. Thanks to recent progress in metamaterials, metasurfaces, epsilon-near-zero materials and plasmonics, many new concepts have been introduced into the design of absorbers [1-11]. In particular, the metamaterial and metasurface concept allows engineering the effective dielectric and magnetic properties by designing the constituent structures. Here we show numerically that a metasurface perfect absorber can be realized by exploiting the guided resonance of a photonic hypercrystal (PHC) — a periodic structure that combines the properties of hyperbolic materials and photonic crystals [12-15].

Hyperbolic materials have attracted a lot of attention because of the various applications associated with the propagating high-k modes and the enhanced photonic density of states [16-18]. As most of the interesting behaviors of hyperbolic materials reside in the propagating high-k modes, however, there is a large k-vector mismatch between the propagating modes in the free space and in a hyperbolic material. This results in difficulties in accessing the high-k modes in hyperbolic materials with simple far-field optics. On the other hand, PHCs can bridge the k-vector mismatch and enable applications that are directly accessible from the far field; this can be performed very efficiently via guided resonance [19-24]. A PHC is essentially a photonic crystal that includes a hyperbolic material as the constituent element [12]. It combines the unique material dispersion of a hyperbolic material with the band formation from the periodic structure. Because of the high-k modes supported in hyperbolic materials, the unit cell of the PHC can have deep subwavelength dimension and still form a photonic band structure. Many interesting applications are enabled by PHCs, including creating Dirac dispersion [13], making better Veselago lenses [14], and enhancing the spontaneous emission of quantum dots [15].

Guided resonance, originating from the resonant coupling to the leaky guided modes, has been exploited extensively in photonic crystals and dielectric gratings [19-24]. Guided resonance provides a route to access efficiently the leaky confined modes from free space. It has been applied to realize perfect absorbers [20], filters, and high reflectors [21]. It has also been used for engineering thermal emission [22] and improving light extraction from light-emitting diodes (LEDs) [23]. In this work, we extend the idea and exploit the guided resonance of a PHC slab. The use of PHC here is particularly attractive because hyperbolic materials are able to support high-k modes, and therefore light can be confined to a thickness much smaller than a wavelength. In fact, we will show that the thickness can be so small that the PHC slab can be treated as a metasurface. Similar deep subwavelength light confinement enabled by hyperbolic materials has been reported in the literature to create three-dimensional resonators with size as small as λ/86 [25,26].

In this work, we show that the PHC slab serves as an angle-insensitive, two-dimensional (2D) resonator, as the field is tightly confined in the thickness direction while more extended in the lateral direction. It can therefore be treated as a metasurface. By incorporating the PHC slab with a dielectric spacer and a back reflector, a Salisbury screen absorber is formed [27]. We show that critical coupling can be obtained in this absorber, which realizes an absorption close to unity [28]. Furthermore, we show that because of the 2D nature, the PHC slab is especially suitable for combining with graphene to enhance the otherwise weak light-graphene interaction. The combined system of a PHC slab and graphene creates an active metasurface that can be tuned by electrical gating [28,29]. In particular, we present examples of such combined systems, including a graphene-PHC optical modulator and

*youchia@umich.edu

graphene photodetectors with enhanced absorption in graphene.

DEVICE STRUCTURE

The PHC-based perfect absorber, as shown by Fig. 1(a), consists of a PHC slab, a dielectric spacer and a metallic back reflector. The PHC slab is formed by a slab of a hyperbolic material and a subwavelength dielectric grating on top. The period of the dielectric grating is chosen to be much larger than the metamaterial limit but much smaller than the free-space wavelength [12]. In this example, we choose the dielectric to be amorphous silicon (with a refractive index of 3.74, lossless [30]) for both the grating and the spacer. We choose the hyperbolic material to be hexagonal boron nitride (h-BN). h-BN has a layered crystal structure similar to graphite, with the layers held together by the weak van der Waals force. As a result, it has very different in-plane and out-of-plane optical phonon frequencies, and becomes a natural type-I hyperbolic material at wavelengths between 12.1 and 13.2 µm, and a type-II hyperbolic material between 6.2 and 7.4 µm [25, 31-33]. The back reflector is made of Au. We design the PHC-based perfect absorber to operate at the wavelengths near 12.6 µm. The period of the Si grating is 590 nm. The thicknesses of the h-BN slab and the spacer are 50 nm and 640 nm, respectively. Other detailed dimensions are listed in the caption of Fig. 1. The proposed PHC-based absorber can potentially be fabricated by sputtering the silicon spacer, transferring the h-BN slab, and sputtering the top silicon layer. The top silicon grating can be defined by electron-beam or photo- lithography followed by dry etching.

(a)

Si grating
h-BN slab
}PHC slab

(b)

Metasurface

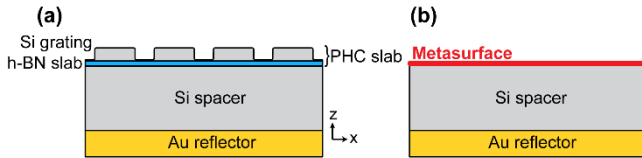Si spacer

Si spacer

Au reflector

Au reflector

z
└→x

FIG. 1. (Color online) (a) The schematic of the PHC-based perfect absorber. The thickness of the h-BN slab (light blue) is 50 nm. The Si grating (light grey) has a period of 590 nm and a duty cycle of 0.68. The heights of the dielectric grating are 130 nm (from the top of the grating to the Si/h-BN interface) and 10 nm (from the valley of the grating to the Si/h-BN interface). The thickness of the dielectric spacer (light grey) is 640 nm. The corners are rounded with a radius of 20 nm in the FEM simulation. (b) The equivalent Salisbury screen absorber, with the PHC slab treated as a metasurface.

The PHC-based absorber is simulated by the full-wave finite-element method (FEM) with a commercial package (COMSOL 5.1). The simulation is further confirmed with the rigorous coupled-wave analysis (RCWA) [34]. The simulated absorption spectrum for the transverse-magnetic (TM) polarization is plotted in Fig. 2, which clearly shows

an absorption of 99.97 % at 12.62 µm. Almost all the absorption is achieved within the very thin h-BN slab (thickness ≈ $\lambda/252$). This is demonstrated by the comparison between the total absorption (blue solid line) and the absorption in Au (magenta solid line) in Fig. 2. h-BN and Au are the only two lossy materials in the simulation, and only a small percentage is absorbed by Au. For comparison, we also simulate the same structure but with the Si grating removed, which exhibits weak and featureless absorption. This reveals the important role played by the periodicity in a PHC. The inset of Fig. 2 plots the absorption at 12.62 µm as a function of the angle of incidence. Interestingly, the response of the PHC-based absorber is insensitive to the angle of incidence. The total absorption remains larger than 98 % up to 45°, which is advantageous for wide-angle applications.
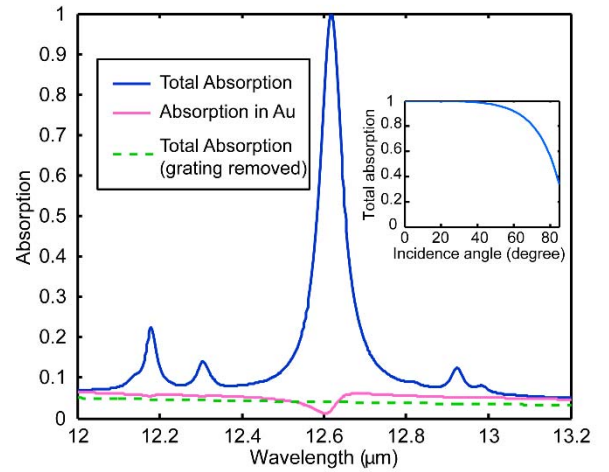

FIG. 2. (Color online) Simulated absorption spectrum of the PHC-based perfect absorber plotted in Fig. 1(a). The simulation is conducted under TM polarization and normal incidence. The total absorption by the entire absorber (blue solid line) is 99.97% at the wavelength of 12.62 µm. h-BN and Au are the only lossy materials in the simulation, and almost all the absorption is achieved by the very thin h-BN slab. The absorption by Au (magenta solid line) is much smaller compared to the total absorption (blue solid line) at resonance. For comparison, we also simulate the same structure but with the Si grating removed (green dash line). The inset shows the angular dependence of the total absorption of the PHC-based absorber evaluated at the wavelength of 12.62 µm.

MECHANISM

A. Guided resonance

The physical origin of the strong absorption can be attributed to the guided resonance of the PHC slab formed by the h-BN slab and the Si grating. Each peak in the absorption spectrum shown in Fig. 2 is associated with a specific waveguide mode of the h-BN slab, and the

presence of the grating perturbs the waveguide mode and turns it into a leaky guided mode. The propagation constant $\beta(\omega)$ of the waveguide modes in a slab of a hyperbolic material in a symmetric cladding environment is given by [35]

$$\frac{\alpha_2/k}{\varepsilon_2/\varepsilon_x} = \tan\left(kh/2\right), \qquad \text{(even modes)} \quad (1a)$$

$$\frac{\alpha_2/k}{\varepsilon_2/\varepsilon_x} = -\cot\left(kh/2\right), \qquad \text{(odd modes)} \quad (1b)$$

where

$$\alpha_2 = \sqrt{\beta^2 - \varepsilon_2\left(\omega/c\right)^2}, \qquad (2a)$$

$$k = \sqrt{\varepsilon_x\left(\omega/c\right)^2 - \left(\varepsilon_x/\varepsilon_z\right)\beta^2}. \qquad (2b)$$

ε_2 is the permittivity of amorphous Si. ε_x and ε_z are the permittivities of h-BN in x- and z-directions. h is the thickness of the h-BN slab. Notice that each mode has two branches, labeled as the backward and the forward branches [30]. The backward branch is tightly confined, and its group velocity and phase velocity have opposite signs, which is an important feature of a type-I hyperbolic waveguide [35]. These waveguide modes have very large β and do not couple to the light in free space. In a PHC, however, the presence of the deep-subwavelength grating enables the coupling to free space and turns the waveguide modes into leaky modes. This is achieved because the grating bridges the in-plane momentum mismatch: $\beta + m\left(2\pi/\Lambda\right) = k_0\sin\theta$, where Λ is the period of the grating, θ is the angle of incidence in free space, and m is an integer.

It can be shown that the perfect absorption is attributed to guided resonance by comparing the field distribution of the PHC-based absorber at the resonance peak with the analytic waveguide mode supported in a hyperbolic slab. This comparison is shown in Fig. 3. The analytic H_y, E_x and E_z fields for the counter-propagating TM$_0$ waveguide modes of the backward branch are plotted in panels (a-c). Panels (d-f) show the FEM simulation of H_y, E_x and E_z fields of the PHC-based perfect absorber at resonance. By comparing Fig. 3 (d-f) with (a-c), it is clear that the guided resonance of the PHC slab originates from the TM$_0$ waveguide mode in the h-BN slab. Other absorption peaks in Fig. 2 are associated with higher-order waveguide modes. Field enhancement (the electric field is enhanced approximately 21 times compared to the incident field) and deep subwavelength confinement are observed inside the h-BN slab at resonance.
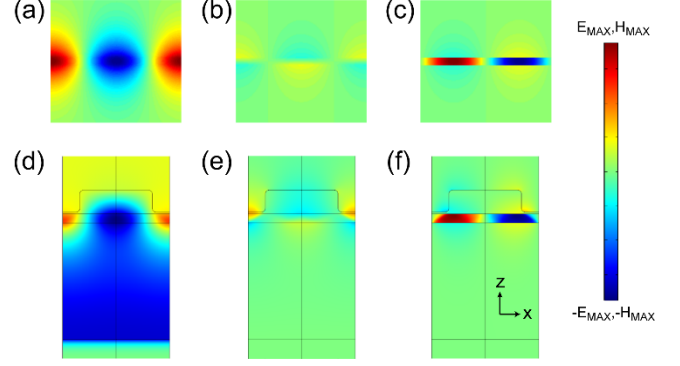

FIG. 3. (Color online) (a) H_y, (b) E_x and (c) E_z of the counter-propagating TM$_0$ waveguide modes (backward branch) in a waveguide of 50nm-thick h-BN slab sandwiched by amorphous silicon at the wavelength of 12.62 μm. (d) H_y, (e) E_x and (f) E_z of the PHC-based perfect absorber simulated using FEM at the wavelength of 12.62 μm. E_x and E_z are plotted with a quarter cycle time difference relative to H_y.

It is worth emphasizing that the period of the PHC is deep subwavelength ($\approx \lambda/21$), in marked contrast to other guided-resonance structures, which often have periods on the order of the wavelength [19-24]. This is a unique feature of PHC, which can be traced back to the high-k modes supported by the hyperbolic material [12]. The angle insensitive response demonstrated by the inset of Fig. 2 is somewhat unexpected at the first glance, as guide-resonance structures are usually angle-sensitive due to the requirement of in-plane momentum match [1]. In PHC, however, because the waveguide mode has an extremely high k-vector, the requirement of in-plane momentum match is achieved almost entirely by the deep subwavelength periodicity of the grating, while the k-vector of the incident wave (which depends on angle) plays little role here.

B. Equivalent metasurface

Because the PHC slab, formed by the Si grating and the h-BN slab, has a deep subwavelength thickness ($\approx \lambda/252$) and period ($\approx \lambda/21$), it can be homogenized and treated as a metasurface. Such a treatment provides an intuitive understanding of the operating principle of the PHC-based absorber and enables straightforward design. Here we apply the method in Ref. [36] to extract the effective parameters of the metasurface from a simulation of the complex reflection and transmission coefficients of the PHC slab. A metasurface can support effective electric and magnetic surface currents, $J_{s,x}$ and $M_{s,y}$, which are given by

$$\begin{pmatrix} J_{s,x} \\ M_{s,y} \end{pmatrix} = \begin{pmatrix} \sigma_e & \chi \\ \chi' & Z_m \end{pmatrix}\begin{pmatrix} E_x \\ H_y \end{pmatrix}, \qquad (3)$$

where σ_e and Z_m are the electric sheet conductivity and magnetic sheet impedance, respectively. χ and χ' are the

magnetoelectric coupling terms. Here we consider only the TM polarization because h-BN exhibits hyperbolic dispersion only in this polarization. These four effective parameters (σ_e, Z_m, χ and χ') describe the properties of the metasurface. To extract these parameters from simulation, we can use the boundary conditions at the interface:

$$-H_y^{(1)} + H_y^{(2)} = J_{s,x} = \sigma_e E_x^{(av)} + \chi H_y^{(av)}$$
$$-E_x^{(1)} + E_x^{(2)} = M_{s,y} = \chi' E_x^{(av)} + Z_m H_y^{(av)} \quad , \quad (4)$$

where the superscripts of (1) and (2) denote the two sides of the metasurface (in our case 1 and 2 refer to air side and Si-spacer side, respectively). The superscript of (av) denotes the average of the two sides. At normal incidence, Eq. (4) can be formulated into an expression that connects σ_e, Z_m, χ and χ' to the S-parameters [36]:

$$\begin{pmatrix} \sigma_e Z_0 \\ \chi \\ \dfrac{Z_m}{Z_0} \\ \chi' \end{pmatrix} = 2 \left(\begin{bmatrix} \mathbf{S} \end{bmatrix} \begin{bmatrix} 0 \end{bmatrix} \\ \begin{bmatrix} 0 \end{bmatrix} \begin{bmatrix} \mathbf{S'} \end{bmatrix} \right)^{-1} \begin{pmatrix} -S_{11}^+ + S_{21} \\ -S_{12} + S_{22}^+ \\ \dfrac{-S_{11}^-}{n_1} - \dfrac{S_{21}}{n_2} \\ \dfrac{-S_{22}^-}{n_2} - \dfrac{S_{12}}{n_1} \end{pmatrix} , \quad (5)$$

where

$$\begin{bmatrix} \mathbf{S} \end{bmatrix} = \begin{pmatrix} \dfrac{S_{11}^-}{n_1} - \dfrac{S_{21}}{n_2} & S_{11}^+ + S_{21} \\ \dfrac{-S_{22}^-}{n_2} + \dfrac{S_{12}}{n_1} & S_{12} + S_{22}^+ \end{pmatrix},$$

$$\begin{bmatrix} \mathbf{S'} \end{bmatrix} = \begin{pmatrix} S_{11}^+ + S_{21} & \dfrac{S_{11}^-}{n_1} - \dfrac{S_{21}}{n_2} \\ S_{12} + S_{22}^+ & \dfrac{-S_{22}^-}{n_2} + \dfrac{S_{12}}{n_1} \end{pmatrix}, \begin{bmatrix} 0 \end{bmatrix} = \begin{pmatrix} 0 & 0 \\ 0 & 0 \end{pmatrix}.$$

The S-parameters are related to the Fresnel reflection and transmission coefficients by $S_{11} = -r_{12}$, $S_{22} = -r_{21}$, $S_{12} = (n_1/n_2) t_{21}$, $S_{21} = (n_2/n_1) t_{12}$. In (5) we additionally introduce $S_{qq}^\pm = S_{qq} \pm 1$, $q = \{1,2\}$. Notice that in the convention of S-parameter S_{mn}, m and n label the receiving and exciting sides, respectively. On the other hand, the opposite convention applies to r_{mn} and t_{mn}, which represent the reflection and transmission coefficients for waves sending from medium m to medium n. The sign of r_{mn} is defined for the electric fields. Temporal dependence in the form of $e^{-i\omega t}$ is assumed.

A full-wave FEM electromagnetic simulation is performed to obtain the reflection and transmission coefficients of the PHC slab alone (the simulation is performed without the back reflector). Using Eq. (5), we can treat the PHC slab as a metasurface and extract the effective parameters. The extracted σ_e, Z_m, χ and χ' are plotted in Fig. 4. We note that $\chi = -\chi'$, which is a consequence of reciprocity. More importantly, it can been seen that the response of the metasurface is dominated by the electric sheet conductivity, since Z_m/Z_0, χ and χ' are all negligible compared to $\sigma_e Z_0$, where Z_0 is the vacuum impedance. Therefore, the PHC slab is effectively an infinitely thin sheet with an electric sheet conductivity σ_e. We will show later in the paper that this gives a quantitatively accurate description for the PHC slab.
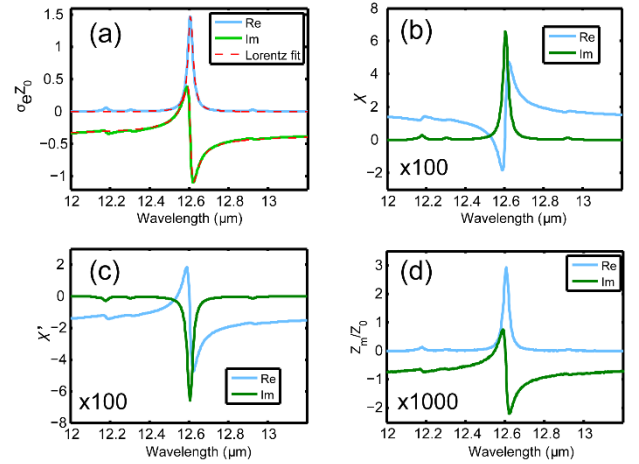

FIG. 4. (Color online) Parameters for the equivalent metasurface of the PHC slab. (a) σ_e, (b) χ, (c) χ', (d) Z_m. Notice that (b) and (c) are scaled by 100 times, and (d) is scaled by 1000 times for clarity. We also perform a Lorenz fit to (a).

The metasurface exhibits the resonant behavior of a Lorentz oscillator, which is shown by Fig. 4(a). We fit the electric sheet conductivity σ_e to this expression:

$$\sigma_e(\omega) = \frac{\sigma_M}{-i(\omega - \omega_0) + \gamma} + ip, \quad (6)$$

where ip is added to account for the constant phase shift due to an effective thickness. Eq. (6) produces a very good fit, from which we extract a quality factor $Q = \omega_0/(2\gamma) = 399$. This value is very close to $\omega(d\varepsilon_z'/d\omega)/(2\varepsilon_z'') = 390$ for h-BN, where ε_z' and ε_z'' are the real and imaginary part of the permittivity of h-BN in z-direction; this is an estimated quality factor obtained simply by assuming the electric field is only in z-direction, entirely inside h-BN, and damped only by the material loss [37].

C. Critical coupling

Since the PHC slab is effectively a metasurface, the absorber can be viewed as a Salisbury screen [27], as plotted in Fig. 1(b), and the resonant metasurface provides the required electric sheet conductivity σ_e for critical coupling. Here we treat the PHC slab as a metasurface with the electric sheet conductivity σ_e only, since other contributions are negligible. The reflection coefficient of the Salisbury screen is given by [28]

$$r = \frac{r_{12} + \left(1 + r_{12} + r_{21}\right)r_{23}e^{i2k_{2Z}d}}{1 - r_{21}r_{23}e^{i2k_{2Z}d}} ,\qquad (7)$$

where r_{23} is the Fresnel reflection coefficient of the Si/Au interface. k_{2Z} is the z component of the wave vector in Si. d is the spacer thickness. The critical coupling condition is satisfied when the numerator of Eq. (7) equals to zero. At normal incidence, we can write down simple analytical expressions for r_{12} and r_{21} using the modified Fresnel equations for an interface with a sheet electric conductivity σ_e [28]:

$$r_{12} = \frac{n_1 - n_2 - \sigma_e Z_0}{n_1 + n_2 + \sigma_e Z_0} ,\qquad (8a)$$

$$r_{21} = \frac{n_2 - n_1 - \sigma_e Z_0}{n_2 + n_1 + \sigma_e Z_0} ,\qquad (8b)$$

where n_1 and n_2 are the refractive indexes for air and Si, respectively. From Eq. (7) and Eq. (8a-b), we can obtain the value of σ_e required for critical coupling:

$$\sigma_e Z_0 = n_1 - n_2 \frac{1 - r_{23}e^{i2k_{2Z}d}}{1 + r_{23}e^{i2k_{2Z}d}} \qquad (9)$$

Therefore, if a metasurface is designed to provide this electric sheet conductivity, perfect absorption can be achieved. This condition can be used to guide the design for the appropriate PHC slab. Eq. (9) is plotted as a function of the spacer thickness d in Fig. 5. Since we cannot obtain arbitrary values for the real and imaginary parts of σ_e with the PHC slab, Fig. 5 suggests that the most practical design for critical coupling is to choose a thickness d not too far from $\lambda/(4n_2) = 844$ nm. With this choice, it is easier to design the PHC slab since the required $\mathrm{Im}\,\sigma_e$ is not too extreme. On the other hand, the required $\mathrm{Re}\,\sigma_e$ is essentially independent of d, according to Fig. 5. Furthermore, because the required $\mathrm{Im}\,\sigma_e$ can be tuned by changing the spacer thickness d, as long as we can design a metasurface with sufficient Lorentz oscillator strength, we can also always find a spacer thickness d to achieve critical coupling.

In Fig. 5 we also mark the σ_e value required for critical coupling when $d = 640$ nm, which is the spacer thickness used in our design of the PHC-based perfect absorber (see the caption of Fig. 1). In the inset, we mark the σ_e provided by the PHC slab, as extracted from the simulation. It can be seen that the PHC slab indeed provides appropriate electric sheet conductivity for critical coupling.
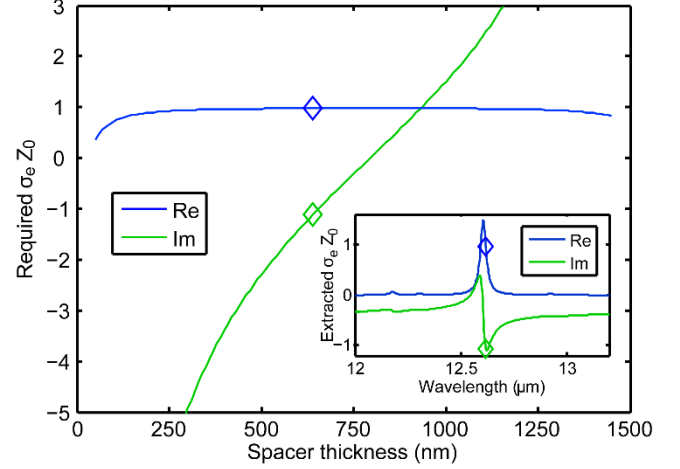

FIG. 5. (Color online) Electric sheet conductivity σ_e required to achieve critical coupling as a function of the spacer thickness. It is plotted for $n_1 = 1$ (air), $n_2 = 3.74$ (amorphous Si) and $n_3 = 11.91 + 89.21i$ (Au) at a wavelength of 12.62 µm. The markers indicate the σ_e value at the spacer thickness of 640 nm, the thickness used in our design shown by Fig. 1(a). The inset shows the effective electric sheet conductivity σ_e provided by the PHC slab (same as Fig. 4), with the σ_e value at the operating wavelength (12.62 µm) of the PHC-based absorber indicated by markers.

We can further verify that that the equivalent Salisbury screen reproduces accurately the behavior of the PHC-based absorber. In Fig. 6(a) we use two different methods to calculate the absorption spectrum of the PHC-based absorber for different spacer thicknesses. The solid lines are obtained with the full-wave FEM simulation of the detailed geometry (i.e. including the grating and h-BN slab). In the same figure, the cross marks are obtained by homogenizing the PHC slab into a metasurface and treating the absorber as a metasurface Salisbury screen, as shown in Fig. 1(b). For the Salisbury screen, the absorption is calculated semi-analytically using Eq. (7) and Eq. (8a-b) together with the extracted electric sheet conductivity σ_e plotted in Fig. 4(a). It can be seen that the semi-analytical calculation of the Salisbury screen reproduces excellently the full-wave simulation of the detailed geometry. Notice that in Fig. 6(a) the critical coupling condition is satisfied when $d = 640$ nm and $\lambda = 12.62$ µm, as well as when $d = 840$ nm and $\lambda = 12.595$ µm.
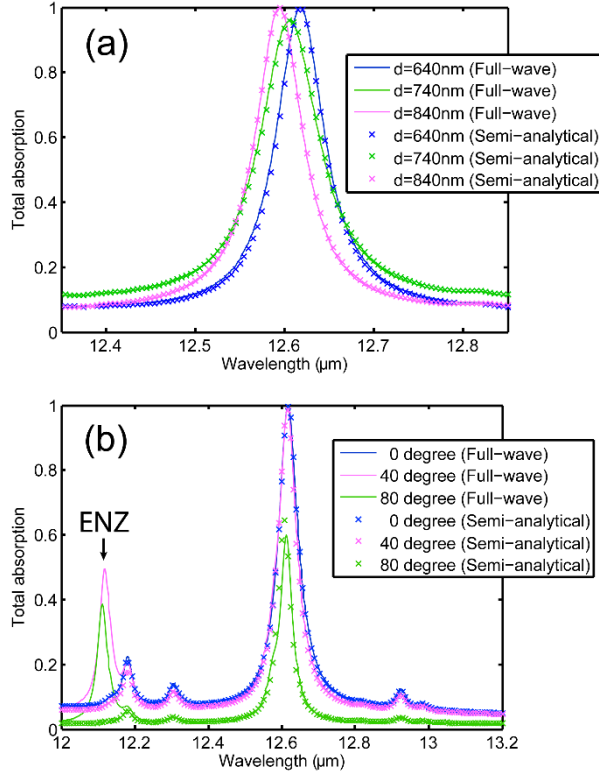
FIG. 6. (Color online) (a) The absorption spectra of the PHC-based absorber with different spacer thicknesses. (b) The absorption spectra of the PHC-based absorber with different incidence angles. The results obtained from both full-wave FEM simulation and semi-analytical calculation are plotted for comparison.

Another verification for the equivalent metasurface Salisbury screen is given by Fig. 6(b). Recall that in Eq. (5) the effective sheet conductivity σ_e is extracted from the simulation performed at normal incidence. Therefore, we still need to check if the σ_e extracted at normal incidence is valid for oblique incident angles. Fig. 6(b) shows the angular dependence of the absorption spectra, obtained by both the full-wave simulation of detailed geometry and the semi-analytical calculation of the equivalent Salisbury screen. As indicated by the results, the semi-analytical calculation reproduces the full-wave simulation very well, except that there is a slight deviation at very large angle, and the semi-analytical calculation misses the peak occurring at the wavelength of 12.1 µm for oblique angles. At this wavelength, h-BN becomes an epsilon-near-zero (ENZ) material, which can offer field enhancement to the z-component of the electric field [38]. The effective metasurface cannot capture this feature because of the lack of out-of-plane response. Nevertheless, this peak associated with ENZ is not relevant to the behavior of the PHC since h-BN is no longer a hyperbolic material at this wavelength.

Our analysis shows that the PHC-based perfect absorber is effectively a Salisbury screen in which the PHC slab serves as a metasurface to provide the appropriate sheet conductivity required for critical coupling, which is given by Eq. (9). This understanding is quantitatively accurate, and can be used as a guidance for designing the PHC-based perfect absorber. More specifically, the appropriate sheet conductivity can be obtained by designing the geometry of the silicon grating. Fig. 7 shows how the sheet conductivity depends on the height, the duty cycle and the period of the silicon grating. The oscillator strength of the resonance can be tuned by the height or the duty cycle [39], while the resonant wavelength can be tuned by the period. Notice that the resonant wavelength blue shifts as the period increases, which is a special feature of a hyperbolic material. The geometry of the silicon grating along with the spacer thickness (as indicated by Fig. 5) provides enough tunability to achieve critical coupling at a desired wavelength.
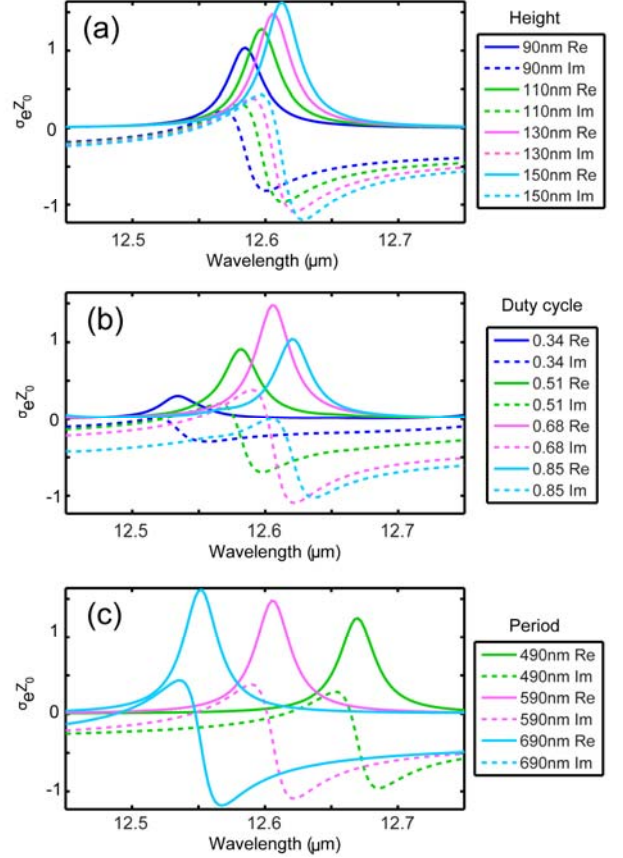

FIG. 7. (Color online) The effective electric sheet conductivity σ_e of the PHC slab obtain with different grating heights (a), duty cycles (b), and periods (c). All other dimensions are kept the same as described in the caption of Fig. 1.

APPLICATIONS

A. Optical modulator

The PHC-based perfect absorber can combine with graphene to make optical modulators, as demonstrated by the inset of Fig. 8. The dimensions of the device structure are the same as those in Fig. 1(a) except that the spacer thickness is changed to 710 nm, since the presence of graphene changes the critical coupling condition. This optical modulator can potentially be fabricated by the same process of fabricating Fig. 1(a) except adding a graphene transfer step. To gate graphene, the silicon spacer can be slightly doped to be part of the gate electrode [40], and the h-BN slab serves as the gate dielectric [41]. Alternatively, we can use intrinsic silicon as the spacer, which becomes part of the gate dielectric. It is also possible to use two graphene layers to sandwich the h-BN slab; in this case the two graphene layers serve as the gate electrodes and the h-BN slab as the gate dielectric [42]. Here we present the simulation results of the device structure plotted in the inset of Fig. 8, which has one graphene layer.

By incorporating the PHC slab with graphene, the effective metasurface becomes dynamically tunable. Because of its atomic thickness, graphene itself does not have enough interaction with light to modulate light effectively, and therefore graphene-based modulators usually need to incorporate resonant structures such as metallic metasurfaces [28], micro rings [42], or patterning of the graphene into a plasmonic structure [43]. Similarly, here the PHC slab serves as a resonant structure to enhance the otherwise weak light-graphene interaction. It should be noted that the PHC slab can work together with graphene very well, because the electric field is tightly confined into a deep subwavelength thickness. It forms a very thin, almost 2D-like cavity that can interact efficiently with 2D materials. This device structure offers several advantages for optical modulation. Because the design utilizes critical coupling, the reflection is minimized when the modulator is in the OFF state, which enables good modulation depth [28,43]. Also, the high mobility of graphene can potentially offer high operation speed, as other graphene-based modulators operating up to 30 GHz have been demonstrated experimentally [28,42]. Furthermore, h-BN is a particularly good match for graphene, since they share very similar lattices such that h-BN helps maintain the high mobility of graphene [44]. Such a graphene-h-BN combined system has been studied in the literature [33,45].
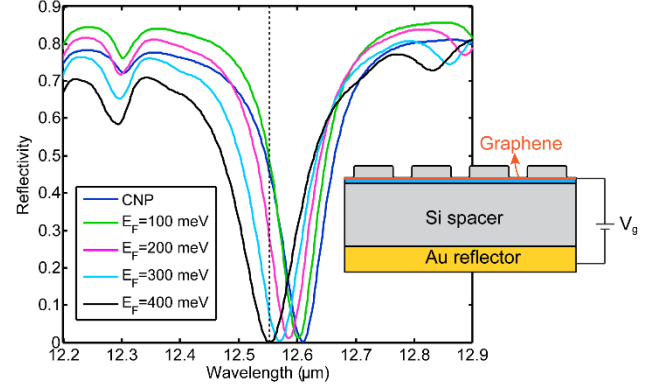

FIG. 8. (Color online) The reflection spectra of the graphene-PHC optical modulator when graphene is gated to different Fermi energies. The dash line marks the operating wavelength at 12.55 µm. E_F = 100 meV and 400 meV correspond to the ON and OFF state of the optical modulator, respectively. The inset shows the device structure.

Fig. 8 shows the calculated reflection spectra of the graphene-PHC optical modulator when graphene is gated to different Fermi energies. To model graphene in the FEM simulation, we assign a surface current at the boundary, with the amplitude proportional to the in-plane electric field. The highest Fermi energy simulated is 400 meV, which is a value often achieved experimentally with electrical gating [43]. The optical conductivity of graphene is simply taken as the universal conductivity $\sigma_0 = e^2/(4\hbar)$ when graphene is gated to the charge neutrality point (CNP). For other Fermi energies, the simulation is done with the optical conductivity model of graphene given by [46-47]

$$
\sigma(\omega) = i \frac{8\sigma_0}{\pi} \frac{k_B T}{\hbar\omega + i\hbar\gamma} \ln\left[2\cosh\left(\frac{E_F}{2k_B T}\right)\right]
$$
$$
+ \frac{4\sigma_0\omega}{i\pi} \int_0^\infty \frac{G(\xi)}{4\xi^2 - \omega^2} d\xi \tag{10a}
$$

where

$$
G(\omega) \triangleq \frac{\sinh\left[\hbar\omega/(k_B T)\right]}{\cosh\left[E_F/(k_B T)\right] + \cosh\left[\hbar\omega/(k_B T)\right]}. \tag{10b}
$$

The first and second terms correspond to the Drude intraband and the interband response, respectively. E_F is the Fermi energy relative to the Dirac point, and γ is the intraband scattering rate. Interband scattering is not included in this expression. We choose T to be 300 K and $\hbar\gamma$ to be 20 meV, which is a reasonable scattering rate for chemical-vapor-deposited (CVD) graphene [48]. In spite of some limitations, such as the need for excitonic corrections in the ultraviolet and visible spectral ranges [49], Eq. (10a)

has been shown experimentally to be a good description for doped graphene in mid-infrared and terahertz ranges [48,50]. Notice that the critical coupling is designed for E_F =400 meV; in this case light is almost perfectly absorbed (absorption = 99.98 %) at the wavelength of 12.55 µm. This optical modulator is designed to operate at a center wavelength of 12.55 µm, and its ON state and OFF state correspond to E_F =100 meV and 400 meV, respectively. The modulation depth, defined by $(1 - R_{OFF}/R_{ON})$, can achieve 99.96 %, where R_{OFF} and R_{ON} are the reflectivities of the OFF and ON state. This good modulation depth is made possible by the critical coupling design that minimizes R_{OFF}. Another figure of merit for optical modulators is the insertion loss, which is defined by $-10 \log R_{ON}$ in the unit of dB. The graphene-PHC optical modulator exhibits an insert loss of 3.2 dB.

B. Absorption enhancement in graphene

The same device structure shown in Fig. 8 can also be used to enhance the absorption in graphene, which can be applied to graphene-based photodetectors and sensors to improve their responsivity. Since the field is confined and enhanced within a deep subwavelength thickness, the PHC slab forms an ultra-thin, 2D-like cavity that enhances the absorption in graphene. This is particularly useful for those detection mechanisms that rely on absorption over the whole area (in contrast to mechanisms relying on junctions), such as bolometric and photogating effects [51,52].
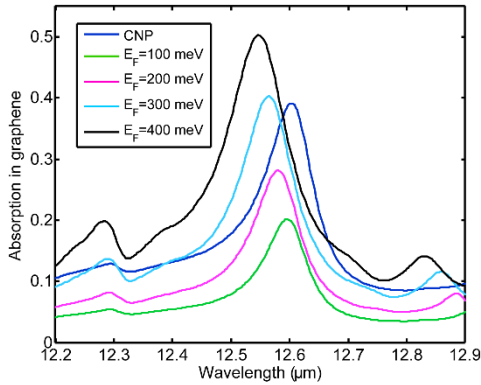

FIG. 9. (Color online) The absorption by the graphene layer for the device plotted in the inset of Fig. 7.

The absorption enhancement is shown in Fig. 9, where we plot the absorption by the graphene for the same device shown by the inset of Fig. 8. It can be seen that, at the CNP, the monolayer graphene can absorb up to 39 % of the light, which is ≈ 17 times enhancement compared to the 2.3% absorption of suspended graphene. This value is larger than the 4-5 times absorption enhancement achieved by optical antennas [53] and slightly smaller than the 26 times

absorption enhancement demonstrated with a microcavity [54].

DISCUSSION

It is worth emphasizing that the PHC slab forms a special resonator with 2D-like nature. The field is tightly confined in the thickness direction (thickness=50 nm) while more extended in the lateral direction (period=590 nm). This is different from resonators based on localized surface plasmons, which are tightly confined in three dimensions, and also different from photonic crystal resonators, which do not have deep subwavelength confinement. We have also shown that it is angle-insensitive, also a dramatic difference from many resonators with extended modes [1].

In this work, h-BN is used as the hyperbolic material. The operating spectral range is restricted to the small spectral window in which h-BN exhibits hyperbolic dispersion. However, there are many other natural hyperbolic materials that cover entire spectrum from ultraviolet to far infrared [32]. Furthermore, the required hyperbolic dispersion can also be obtained with hyperbolic metamaterials (HMMs), which can be engineered for the desired spectral range [16-18,48]. Another restriction of the current design of the PHC-based absorber is the polarization. It works only for TM polarization due to the use of the one-dimensional grating structure. The current design can potentially be extended to make polarization-independent perfect absorbers with 2D periodic structures such as disc or hole arrays.

CONCLUSION

In summary, we have reported a numerical study of a perfect absorber based on the guided resonance of a PHC. We have shown that, by a careful design of the PHC slab, we can couple light resonantly from the free space to a specific leaky guided mode, which has a deep subwavelength confinement in the thickness direction. Therefore, the PHC slab can serve as a 2D-like resonator, which can be treated accurately as a metasurface. The effective electric sheet conductivity of the PHC slab is extracted from the simulation. We have also shown that the perfect absorber, consisting of a PHC slab, a dielectric spacer and a back reflector, is equivalent to a metasurface Salisbury screen. The critical coupling condition for this absorber is discussed. In addition, we have demonstrated that this absorber can be particular useful to combine with graphene because of the 2D-like nature of the PHC slab. Applications of such combined systems in optical modulators and graphene detectors are discussed.

[1] Y. Cui, Y. He, Y. Jin, F. Ding, L. Yang, Y. Ye, S. Zhong, Y. Lin, and S. He, Laser Photon. Rev. **8,** 495 (2014).

[2] Y. Ra'di, C. R. Simovski, and S. A. Tretyakov, Phys. Rev. Applied **3,** 037001 (2015).

[3] C. M. Watts, X. Liu, and W. J. Padilla, Adv. Mater. **24,** OP98 (2012).

[4] M. A. Kats, R. Blanchard, P. Genevet, and F. Capasso, Nat. Mater. **12,** 20 (2013).

[5] K. Aydin, V. E. Ferry, R. M. Briggs, and H. A. Atwater, Nat. Commun. **2,** 517 (2011).

[6] D. Ji, H. Song, X. Zeng, H. Hu, K. Liu, N. Zhang, and Q. Gan, Sci. Rep. **4,** 4498 (2014).

[7] S. Feng, and K. Halterman, Phys. Rev. B **86,** 165103 (2012).

[8] T. S. Luk *et al.,* Phys. Rev. B **90,** 085411 (2014).

[9] J. Yoon *et al.,* Sci. Rep. **5,** 12788 (2015).

[10] S. Campione, I. Kim, D. de Ceglia, G. A. Keeler, and T. S. Luk, Opt. Express **24,** 18782 (2016).

[11] T. Y. Kim, M. A. Badsha, J. Yoon, S. Y. Lee, Y. C. Jun, and C. K. Hwangbo, Sci. Rep. **6,** 22941 (2016).

[12] E. E. Narimanov, Phys. Rev. X **4,** 041014 (2014).

[13] E. E. Narimanov, Farad. discuss. **178,** 45-59 (2015).

[14] Z. Huang and E. E. Narimanov, Appl. Phys. Lett. **105,** 031101 (2014).

[15] T. Galfsky, E. E. Narimanov, and V. Menon, in *Frontiers in Optics*, OSA Technical Digest (online) (Optical Society of America, 2015), paper FW6A.3.

[16] D. R. Smith and D. Schurig, Phys. Rev. Lett. **90,** 077405 (2003).

[17] A. Poddubny, I. Iorsh, P. Belov, and Y. Kivshar, Nat. Photon. **7,** 948 (2013).

[18] Z. Jacob, J. Y. Kim, G. V. Naik, A. Boltasseva, E. E. Narimanov, and V. M. Shalaev, Appl. Phys. B **100,** 215 (2010).

[19] S. Fan and J. D. Joannopoulos, Phys. Rev. B **65,** 235112 (2002).

[20] J. R. Piper and S. Fan, ACS Photon. **1,** 347 (2014).

[21] Y. Ding and R. Magnusson, Opt. Express **12,** 5661 (2004).

[22] T. Inoue, M. De Zoysa, T. Asano, and S. Noda, Nat. Mater. **13,** 928 (2014).

[23] N. Ganesh, W. Zhang, P. C. Mathias, E. Chow, J.A.N.T. Soares, V. Malyarchuk, A.D. Smith, and B.T Cunningham, Nat. Nanotechnol. **2,** 515 (2007).

[24] D. de Ceglia, M. A. Vincenti, M. Grande, G. V. Bianco, G. Bruno, A. D'Orazio, and M. Scalora, J. Opt. Soc. Am. B **33,** 426 (2016).

[25] J.D. Caldwell *et al.,* Nat. Commun. **5,** 5221 (2014).

[26] X. Yang, J. Yao, J. Rho, X. Yin, and X. Zhang, Nat. Photon. **6,** 450 (2012).

[27] W. W. Salisbury, U.S. Patent No. 2,599,944, 10 June, 1952.

[28] Y. Yao, R. Shankar, M. A. Kats, Y. Song, J. Kong, M. Loncar, and F. Capasso, Nano Lett. **14,** 6526 (2014).

[29] J. Park, J. H. Kang, X. Liu, and M. L. Brongersma, Sci. Rep. **5,** 15754 (2015).

[30] E. D. Palik, *Handbook of optical constants of solids* (Academic Press, San Diego, 1985), Vol. 1.

[31] P. Li, M. Lewin, A.V. Kretinin, J.D. Caldwell, K.S. Novoselov, T. Taniguchi, K. Watanabe, F. Gaussmann, and T. Taubner, Nat. Commun. **6,** 7507 (2015).

[32] E. E. Narimanov and A. V. Kildishev, Nat. Photon. **9,** 214 (2015).

[33] S. Dai *et al.*, Nat. Nanotechnol. **10,** 682-686 (2015).

[34] V. Liu and S. Fan, Comput. Phys. Commun. **183,** 2233 (2012).

[35] H. Hu, D. Ji, X. Zeng, K. Liu, and Q. Gan, Sci. Rep. **3,** 1249 (2013).

[36] C. Pfeiffer and A. Grbic, Phys. Rev. Applied **2,** 044011 (2014).

[37] F. Wang and Y. R. Shen, Phys. Rev. Lett. **97,** 206806 (2006).

[38] S. Molesky, C. J. Dewalt, and Z. Jacob, Opt. Express **21,** A96 (2013).

[39] T. Tamir, and S. T. Peng. Appl. Phys. **14,** 235-254 (1977).

[40] M. Liu, X. Yin, E. Ulin-Avila, B. Geng, T. Zentgraf, L. Ju, F. Wang, and X. Zhang, Nature **474,** 64 (2011).

[41] I. Meric, C. R. Dean, N. Petrone, L. Wang, J. Hone, P. Kim, and K. L. Shepard, Proc. IEEE **101,** 1609 (2013).

[42] C. T. Phare, Y. H. D Lee, J. Cardenas, and M. Lipson, Nat. Photon. **9,** 511 (2015).

[43] M.S. Jang, V.W. Brar, M.C. Sherrott, J. J. Lopez, L. Kim, S. Kim, M. Choi, and H. A. Atwater, Phys. Rev. B **90,** 165409 (2014).

[44] C. R. Dean, A. F. Young, I. Meric, C. Lee, L. Wang, S. Sorgenfrei, K. Watanabe, T. Taniguchi, P. Kim, K. L. Shepard, and J. Hone, Nat. Nanotechnol. **5,** 722 (2010).

[45] A. Kumar, T. Low, K. H. Fung, P. Avouris, and N. X. Fang, Nano Lett. 15, 3172 (2015).

[46] L. A. Falkovsky and A. A. Varlamov, Eur. Phys. J. B **56**, 281 (2007).

[47] L. A. Falkovsky and S. S. Pershoguba, Phys. Rev. B **76**, 153410 (2007).

[48] Y. C. Chang, C. H. Liu, C. H. Liu, S. Zhang, S. R. Marder, E. E. Narimanov, Z. Zhong, and T. B. Norris, Nat. Commun. **7,** 10568 (2016).

[49] K. F. Mak, J. Shan, and T. F. Heinz, Phys. Rev. Lett. **106,** 046401 (2011).

[50] H. Yan *et al.*, Nat. Nanotechnol. **7,** 330 (2012).

[51] J. Yan, M. H. Kim, J. A. Elle, A. B.Sushkov, G. S. Jenkins, H. W. M. Milchberg, M. S. Fuhrer, and H. D. Drew, Nat. Nanotechnol. **7,** 472 (2012).

[52] C. H. Liu, Y. C. Chang, T. B. Norris, and Z. Zhong, Nat. Nanotechnol. **9,** 273 (2014).

[53] Y. Yao, R. Shankar, P. Rauter, Y. Song, J. Kong, M. Loncar, and F. Capasso, Nano Lett. **14,** 3749 (2014).

[54] M. Furchi *et al.*, Nano Lett. **12,** 2773 (2012).